PCCP

ROYAL SOCIETY OF CHEMISTRY

PAPER

View Article Online
View Journal | View Issue

Cite this: *Phys. Chem. Chem. Phys.*, 2024, **26**, 20672

Unveiling the photophysical and excited state properties of multi-resonant OLED emitters using combined DFT and CCSD method†

Pandiyan Sivasakthi [ab] and Pralok K. Samanta [*ab]

Received 13th February 2024,
Accepted 11th June 2024

DOI: 10.1039/d4cp00637b

rsc.li/pccp

Multi-resonance thermally-activated delayed fluorescence (MR-TADF) is predominantly observed in organoboron heteroatom-embedded molecules, featuring enhanced performance in organic light-emitting diodes (OLEDs) with high color purity, chemical stability, and excellent photoluminescence quantum yields. However, predicting the impact of any chemical change remains a challenge. Computational methods including density functional theory (DFT) still require accurate descriptions of photophysical properties of MR-TADF emitters. To circumvent this drawback, we explored recent investigations on the **CzBX** (Cz = carbazole, X = O, S, or Se) molecule as a central building block. We constructed a series of MR-TADF molecules by controlling chalcogen atom embedding, employing a combined approach of DFT and coupled-cluster (CCSD) methods. Our predicted results for MR-TADF emitter molecules align with the reported experimental data in the literature. The variation in the positions of chalcogen atoms embedded within the **CzBX2X** framework imparts unique photophysical properties.

1. Introduction

In recent years, pure organoboron molecules with heteroatoms are attractive candidates that are receiving considerable attention and are a hot topic of research because of their narrowband emissive property, purity of color, and versatile applications in fields such as optoelectronic devices, photocatalytic synthesis, quantum information technologies, and organic light-emitting diodes (OLEDs).[1–8] Researchers are particularly focused on the characteristics of triplet excited states to enhance the luminescence efficiency.[9–16] The conversion between singlet and triplet states occurs through intersystem crossing (ISC) and reverse intersystem crossing (RISC), respectively, with these processes playing a pivotal role in achieving a high quantum yield for the luminescence process.[17–19] Efficient ISC and RISC processes efficiently occur for low energy gap (ΔE_{ST}) between the lowest excited singlet (S_1) and the lowest excited triplet energy (T_1) states. $\Delta E_{ST} < \sim 0.3$ eV promotes the molecule's role as a thermally-activated delayed fluorescence (TADF) emitter. The TADF mechanism involves the thermal up-conversion of triplet excitons into singlets *via* RISC.[19–23] Conversely, if ΔE_{ST} exceeds ~ 0.4 eV, delayed luminescence at room temperature is most likely due to the room temperature phosphorescence (RTP) and triplet–triplet annihilation (TTA).[24–29] Rate constants for RISC (k_{RISC}) and ISC (k_{ISC}) are intrinsic characteristics dependent on their electronic structure and configuration of molecules. The interplay between the lowest energy gap (ΔE_{ST}) and high spin–orbit coupling (SOC) between the singlet and triplet excited states are two important factors that determine the path for the RISC and ISC processes. To harvest the lowest excited states (*i.e.*, ISC for $S_1 \rightarrow T_n$ and RISC for $T_1 \rightarrow S_1$ conversion), a strong SOC matrix element (SOCME) is essential. In the case of MR-TADF, the rate of RISC is a key factor for efficiently harvesting triplet excitons and thereby converting them into radiative singlet excitons to achieve an internal quantum efficiency (IQE) of $\sim 100\%$.[30,31] In some rare cases of MR-TADF molecules, where the S_1 state energy is close to the energies of two triplets (T_1 and T_2) with a low $\Delta E_{S_1-T_n} < 0.25$ eV, the T_1 exciton can also be harvested *via* RISC from $S_1 \leftarrow T_2$.[32] Hatakeyama *et al.* observed MR-TADF features in DABNA derivatives containing boron and nitrogen atoms.[33] Although the k_{RISC} was initially slow, it was improved significantly in recently developed MR-TADF materials.[9,34–37] A narrow full-width at half-maximum (FWHM) of less than 35 nm is beneficial for enhancing the spectral purity.[38–40]

[a] *Department of Chemistry, Birla Institute of Technology and Science (BITS) Pilani, Hyderabad Campus, Hyderabad-500078, India.*
E-mail: pralokkumar.samanta@hyderabad.bits-pilani.ac.in, pralok.samanta@gmail.com
[b] *Department of Chemistry, School of Science, GITAM University, Hyderabad-502329, India*

† Electronic supplementary information (ESI) available: STEOM-DLPNO-CCSD computational details, structural details, excited state energy using different DFT functional, HOMO, LUMO, ΔE_{H-L}, configurations percentage, and calculated fluorescence and phosphorescence rate constants (pdf). See DOI: https://doi.org/10.1039/d4cp00637b

Extending the molecule (donor–acceptor) or introducing substitution (heavy atoms) gradually increases the performance and reduces the FWHM value.[38–40] Recent studies by Park *et al.* explored organoboron emitters doped with chalcogens to enhance the MR-TADF property for achieving excellent color purity and high luminescence efficiency.[41] Using the design concept by Hatakeyama *et al.*, featuring the MR effects as a new approach to the development of narrowband TADF emitters, MR-TADF molecules used polyaromatic compounds based on organoboron.[33] Hatakeyama and others have introduced a new strategy for the design of embedding methods in organoboron-based polyaromatic molecules.[42–45] Organoboron-based polyaromatic adjacent phenyl units have two hydrogen bonds converted to a heavy atom or chalcogen atom bond in MR-TADF molecules, and this type of embedded molecule shows excellent performance in OLEDs.[34,44–46] Moreover, Park *et al.* identified a novel ideal superimposed fluorescence mechanism for the **CzBSe** molecule, exhibiting a high k_{RISC} up to $\sim 10^8$ s^{-1}. The k_{RISC} significantly increases with an upsurge in the chalcogen atomic number (9.0×10^3, 4×10^5 and 1.5×10^8 s^{-1} for O, S and Se, respectively) in toluene solvent.[41] In this article, we unravel the photophysical properties of the recently published **CzBX** (X = O, S, or Se) molecules and successfully reproduced the experimental data with the combined DFT and CCSD approach results.[47,48] The chalcogen-embedded framework for **CzBX2X** molecules significantly improved the narrowband emission and optical properties. In addition to that, we investigated a comparative study of the MR-TADF **CzBX** skeleton molecules: **CzBO** (5-oxa-8*b*-aza-15*b*-borabenzo[*a*]naphtho[1,2,3-*hi*]aceanthrylene), **CzBS** (5-thia-8*b*-aza-15*b*-borabenzo[*a*]naphtho[1,2,3-*hi*]aceanthrylene) and **CzBSe** (5-selena-8*b*-aza-15*b*-borabenzo[*a*]naphtho[1,2,3-*hi*]aceanthrylene). We also proposed and calculated the photophysical and excited properties of a series of **CzBX2X**-type MR-TADF molecules by controlling chalcogen atom embedding: **CzBO2O** (6,10,13-trioxa-3*a*2-aza-5*a*2-boraindeno[1,2,3,4-*pqra*]naphtho[3,2,1,8-*ghij*]-perylene), **CzBO2S** (10-oxa-6,13-dithia-3*a*2-aza-5*a*2-boraindeno-[1,2,3,4-*pqra*]naphtho[3,2,1,8-*ghij*]perylene), **CzBO2Se** (10-oxa-6,13-diselena-3*a*2-aza-5*a*2-boraindeno[1,2,3,4-*pqra*]naphtho[3,2,1,8-*ghij*]perylene), **CzBS2O** (6,13-dioxa-10-thia-3*a*2-aza-5*a*2-boraindeno[1,2,3,4-*pqra*]naphtho[3,2,1,8-*ghij*]perylene), **CzBS2S** (6,10,13-trithia-3*a*2-aza-5*a*2-boraindeno[1,2,3,4-*pqra*]naphtho[3,2,1,8-*ghij*]-perylene), **CzBS2Se** (10-thia-6,13-diselena-3*a*2-aza-5*a*2-boraindeno[1,2,3,4-*pqra*]naphtho[3,2,1,8-*ghij*]perylene), **CzBSe2O** (6,13-dioxa-10-selena-3*a*2-aza-5*a*2-boraindeno[1,2,3,4-*pqra*]naphtho-[3,2,1,8-*ghij*]perylene), **CzBS2S** (6,13-dithia-10-selena-3*a*2-aza-5*a*2-boraindeno[1,2,3,4-*pqra*]naphtho[3,2,1,8-*ghij*]perylene) and **CzBSe2Se** (6,10,13-triselena-3*a*2-aza-5*a*2-boraindeno[1,2,3,4-*pqra*]-naphtho[3,2,1,8-*ghij*]perylene) (see Fig. 1).

2. Theoretical methodology and computational details

2.1 Geometries optimization and optical absorption

Ground state (S_0) optimizations were carried out using density functional theory (DFT) employing the optimally tuned screened range-separated hybrid (OT-SRSH)[15,49,50] ωB97XD functional (ω values are listed in Table S1a, ESI†) and 6-31G(d) basis set for H, B, C, N, O and S atoms except for Se atom, for which the ECP (effective core potential) type basis set LANL2DZ was used. Excited state geometry optimizations were performed using time-dependent DFT (TDDFT) method with OT-SRSH-ωB97XD functional with the abovementioned basis set. The toluene solvent was modeled with polarizable continuum model (PCM) with dielectric constant (ε) = 2.3741 to compare with the reported experimental data available in the literature.[51] For TDDFT calculations, Tamm–Dancoff approximation (TDA) were considered to avoid triplet instability.[49] The range-separation parameter, ω for OT-SRSH-ωB97XD functional was determined by minimizing J^2 as follows.[52–54]

$$J^2 = \sum_{i=0}^{1} |\varepsilon_H(N+i) + IP(N+i)|^2 \quad (1)$$

where IP and ε_H denote the ionization potential and HOMO (highest occupied molecular orbital) energy of a given molecule, respectively, and N is the number of electrons in the molecule. All the DFT and TDDFT calculations mentioned above were carried out with the Gaussian 16 software.[55] In a previous study, Olivier and coworkers showed that linear-response DFT approaches consistently overestimate the ΔE_{ST} gaps in MR-TADF molecules.[56] We carried out similarity transformed equation-of-motion coupled-cluster (with single and double excitations) method augmented with domain-based on local pair natural orbitals (STEOM-DLPNO-CCSD), which is a highly correlated wave function-based approach. It offers an accurate treatment for the excited state characteristics of various molecules, including MR-TADF molecules. These wavefunction-based calculations were performed with def2-TZVP basis set, as implemented in the ORCA V5.0.3 package.[57,58] To avoid prohibitive computational costs, the energies of the singlet and triplet states and the related ΔE_{ST} values were calculated using STEOM-DLPNO-CCSD/def2-TZVP on the basis of the excited-state geometries (for S_1, T_1 and T_2) obtained using the OT-SRSH-ωB97XD/6-31G(d)/LANL2DZ level of theory. This protocol provides manageable computational costs, while accurately reproducing the experimental data reported for known MR-type molecules.[59,60] Thus, in our combined DFT and CCSD method, we used the OT-SRSH-ωB97XD/6-31G(d)/LANL2DZ level of theory for geometry optimization and STEOM-DLPNO-CCSD/def2-TZVP level of theory for single-point energy calculation. Vertical excitation calculation of STEOM-DLPNO-CCSD configuration details is provided in the ESI.†

2.2 Intersystem crossing (ISC) rate

The rate constant for the ISC process from $S_1 \rightarrow T_n$ conversions and RISC process from T_1 or $T_2 \rightarrow S_1$ conversions were calculated using the Fermi's Golden Rule[61,62]

$$k^n_{ISC/RISC} = \frac{2\pi}{\hbar}\rho_{FC}\left|\langle S_1|\hat{H}_{SOC}|T_n\rangle\right|^2 \quad (2)$$

where $\langle S_1|\hat{H}_{SOC}|T_n\rangle$ and ρ_{FC} denote the spin–orbit coupling matrix element (SOCME) between the S_1 and T_n state and Franck–Condon weighted density of states, respectively. We used

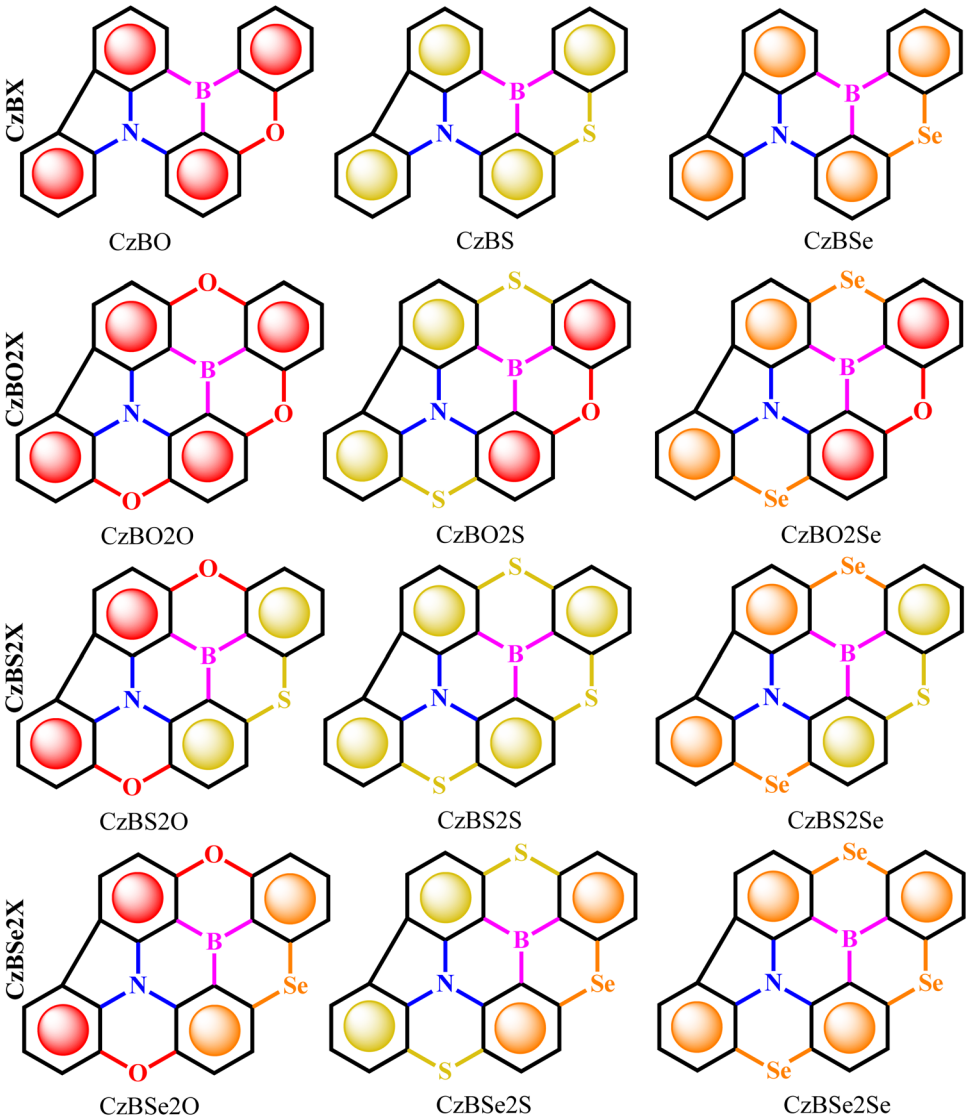

Fig. 1 Chemical structures of the **CzBX** and **CzBX2X** series are investigated in this work where X = O, S and Se. **CzBX** molecules are experimentally reported before, and **CzBX2X** molecules are proposed in this work.

optimized excited state geometry (T_1, T_2-state optimized geometry for RISC and S_1 state optimized geometry for ISC) obtained using OT-SRSH-ωB97XD/6-31G(d)/LANL2DZ//STEOM-DLPNO-CCSD/def2-TZVP (DFT-CCSD) for the calculation of the SOCME between the S_1, T_1 and T_2 states. According to the Franck–Condon principle, electronic transition happens first and then relaxation of the geometry occurs. Thus, we considered the T_1, T_2-state optimized geometry for the calculation of the SOCME between the S_1 and T_1, and S_1 and T_2 states as we studied the transition (*i.e.*, ISC and RISC) from the T_1, T_2 state to S_1 state (RISC), and S_1 state to T_1, T_2 state (ISC). The ρ_{FC} was estimated using the Marcus–Levich–Jortner theory.[63]

$$\rho_{FC} = \frac{1}{\sqrt{4\pi\lambda_M k_B T}} \sum_{n=1}^{\infty} \exp(-S)\frac{S^n}{n!} \exp\left[-\frac{(\Delta E_{ST} + n\hbar\omega + \lambda_M)^2}{4\lambda_M k_B T}\right] \quad (3)$$

where λ_M is the reorganization energy, k_B is the Boltzmann constant, T is the absolute temperature, S is the effective Huang–Rhys factor (S) associated with non-classical high-frequency intramolecular vibrational modes, and we found that S is less than 0.05 and the RMSD is less than 0.04 Å between the S_1 and T_1 optimized geometries. Thus, the reorganization energy between the S_1 and T_1 optimized geometries tends to zero (see Table S1b, ESI†). Thus, the S values were considered to be zero. The total reorganization energy has two components: the intramolecular reorganization energy is ~0.006 eV (see Table S1c, ESI†) and the contribution of reorganization energy from the surroundings and solvent effect approximated to 0.2 eV. It is worthy to note that $\Delta E_{ST} = \Delta E_{S_1-T_n}$ for the ISC process whereas $\Delta E_{ST} = \Delta E_{T_n-S_1}$ for the RISC process. We used our own FORTRAN code to calculate $k_{RISC/ISC}$ using eqn (2) and (3) (available on https://Github.Com/Pralok87/Fortran-Code-for-ISC (**https://Github.Com/Pralok87/Fortran-Code-for-ISC**)). The overall intersystem crossing

rate constant (k_{ISC}) from the excited S_1 state to the triplet manifold (T_m) is given by[63]

$$k_{ISC} = \sum_m k_{ISC}^m \quad (4)$$

2.3 Fluorescence and phosphorescence rate

The fluorescence and phosphorescence calculations were done based on excited state geometries optimized using the OT-SRSH-ωB97XD/6-31G(d)/LANL2DZ method. In order to account for the solvent effect, the toluene conductor-like polarizable continuum model (CPCM) was used. The fluorescence rate constants (k_r) were calculated using Einstein A coefficient[63,64]

$$k_r = A_{fi} = \frac{(E_f - E_i)^3}{3\varepsilon_0 \pi \hbar^4 c^3} |\langle f|\hat{\mu}|i\rangle|^2 \quad (5)$$

where E_f and E_i are the energies of the excited (f) and ground states (i), respectively, and $f|\hat{\mu}|i$ is the corresponding transition–dipole moment.

The phosphorescence rate constant, k_{ph} and radiative lifetime τ_{ph} from each sublevel i (i = I, II, III) of the T_1 state to the ground S_0 state were calculated by making use of the transition energy ΔE_i and the transition dipole moment $\boldsymbol{M}_i$, as defined in eqn (6)[65,66]

$$k_i = \frac{1}{\tau_i} = \frac{4}{3t_0}\alpha_0^3 (\Delta E_i)^3 \sum_{\alpha=x,y,z} |M_\alpha^i|^2 \quad (6)$$

where $t_0 = (4\pi\varepsilon_0)^2\hbar^3/m_e e^4$. ε_0, $\hbar$, m_e, e and α_0 are the vacuum permittivity, reduced Planck constant, electron mass, electron charge and the fine structure constant, respectively. The contribution to the transition moment was calculated from the first-order (higher order is neglected in this study) corrected wave functions. The sublevels of the triplet state are considered to be energy degenerate; thus, the final expression for M_α^i is

$$M_\alpha^i = \sum_{n=0}^{\infty} \frac{\langle S_0|\hat{\mu}_\alpha|S_n\rangle\langle S_n|\hat{H}_{SOC}|T_1^i\rangle}{E(S_n) - E(T_1)} + \sum_{n=1}^{\infty} \frac{\langle S_0|\hat{H}_{SOC}|T_n\rangle\langle T_n|\hat{\mu}_\alpha|T_1^i\rangle}{E(T_n) - E(S_0)} \quad (7)$$

The transition dipole moment operator $\hat{\mu}$ can be expanded in terms of vibrational normal modes.[67,68]

$$\widehat{\mu(Q)} = \hat{\mu}_0 + \sum_k \left(\frac{\partial \hat{\mu}}{\partial Q_k}\right)_{Q_k=0} Q_k + \mathcal{O}(Q_k^2) \quad (8)$$

The first order correction term (*i.e.*, the Herzberg–Teller (HT) term) was taken into account in eqn (8) as it can significantly impact the spectra and rate constant calculations.[69] For the calculation of k_F and k_{ph}, we considered the adiabatic hessian (HESSFLAG AH) method along with the Cartesian coordinate systems using the excited state dynamics (ESD) module of the ORCA package.[68,70] A broadening parameter of 200 cm^{-1} was used. Both the emission calculations were done using the OT-SRSH-ωB97XD and def2-TZVP basis set as implemented in the ORCA V5.0.3 package.[58]

We note that the computational methodology used here works relatively well as we compared our calculated results with the available experimentally reported data. The harmonic approximation to the vibrational normal modes works well for the calculation of radiative rate constant, but it is more prone to errors for the calculation of non-radiative rate constants.[68] However, the approximation works well for present molecules due to the less structural relaxation of their ground and excited states optimized geometries. Also, the PCM solvent (toluene) model was used to mimic the surrounding environment effect in the bulk. As the properties of any thin film depends on its thickness, it is difficult to mimic the properties of thin films in reality.

3. Results and discussion

3.1 Structural and electronic properties

The optimized geometrical parameter of the ground-state (S_0) shows the accuracy of the experimental molecule nature. The bond lengths and angles of **CzBX** (X = O, S, or Se) molecules well match with that of the experimental single crystal structure (CIF).[41] The bond lengths of carbon and chalcogen atoms (C–X, X = O, S, Se) are 1.37, 1.75 and 1.90 Å, as reported in the experimental study, and are well comparable with our predicted results of 1.36, 1.77 and 1.89 Å, respectively. The bond lengths between the boron and carbon (C–B) bonds are ∼1.54–1.56 Å. The distance between the carbon and nitrogen (C–N) atoms are ∼1.40–1.43 Å and are well comparable with the reported experimental data (see Table 1 and Fig. 2). The angle of CXC, CBC and CNC decreased correspondingly to the chalcogen atoms.

The HOMO and LUMO (lowest unoccupied molecular orbital) energy levels and their associated ΔE_{H-L} help to explain the origins of the energy shifts of the singlet and triplet states upon the substitution of O, S and Se. In **CzBX**-type molecules, both the HOMO and LUMO energies decrease in the order O, S and Se (E_{HOMO} = −7.537, −7.421 and −7.408 eV; E_{LUMO} = 1.183, 1.111 and 1.081 eV, respectively, see Table S2, ESI†). The HOMO and LUMO gap (ΔE_{H-L}) decreases in the same order (8.720, 8.532 and 8.489 eV for O, S and Se, respectively). It is the reason behind the red shift in the S_1 and T_1 energies going from O to S and Se for **CzBX** molecules (see Fig. 3). The results can be explained from the electronegativity of the chalcogen atoms. A similar observation was found for doubly substituted chalcogens **CzBX2X** series, following the same trend (see Table S2, ESI†).

3.2 Excited state optical properties

The calculated photophysical properties of the **CzBX** molecules are compared with the available experimental data (see Table 2). The UV-visible absorption spectrum calculated for the **CzBX** molecules exhibits a characteristic spectral signature with the lowest energy absorption maximum (λ_{abs}^{max}) in the range of 422–450 nm. For the **CzBO** molecule, the calculated λ_{abs} is 422 nm (f = 0.3415), which is well comparable with the experimental results (λ_{abs} is 426 nm). On the other hand, the calculated λ_{abs}^{max} for S and Se substituted for the **CzBS** molecules

Table 1 Comparison data from the experimental single crystal structure and theoretically optimized (OT-SRSH-ωB97XD/6-31G(d)/LANL2DZ) geometry

Molecules	C–X[a]	C–X[b]	C–B[c]	C–B[d]	C–N[e]	C–N[f]	CXC[g]	CBC[h]	CBC[i]	CNC[j]	CNC[k]
Expt.[41]											
CzBO	1.37	1.38	1.54	1.55	1.41	1.43	122.2	114.7	130.6	121.5	130.5
CzBS	1.75	1.75	1.55	1.56	1.41	1.42	106.8	114.1	125.6	121.2	130.6
CzBSe	1.90	1.90	1.54	1.54	1.41	1.43	101.8	113.9	123.9	120.7	129.9
Calculated results											
CzBO	1.36	1.37	1.53	1.55	1.40	1.41	122.7	114.6	130.7	121.6	130.2
CzBS	1.77	1.77	1.55	1.55	1.40	1.41	106.0	114.4	125.7	121.2	130.3
CzBSe	1.89	1.89	1.55	1.55	1.40	1.41	102.6	114.2	124.2	121	130.4

[a] Carbon and chalcogen atom distance. [b] Carbon and chalcogen atom distance. [c] Carbon and boron atom distance. [d] Carbon and boron atom distance. [e] Carbon and nitrogen atom distance. [f] Carbon and nitrogen atom distance. [g] Angle of carbon, chalcogen and carbon atoms. [h] Angle of carbon, boron and carbon atoms. [i] Angle of carbon, boron and carbon atoms. [j] Angle of carbon, nitrogen and carbon atoms. [k] Angle of carbon, nitrogen and carbon atoms.Distances are given in Å and angles are given in degrees. See Fig. 2 for angles and distances mentioned in footnotes *a*–*k*.

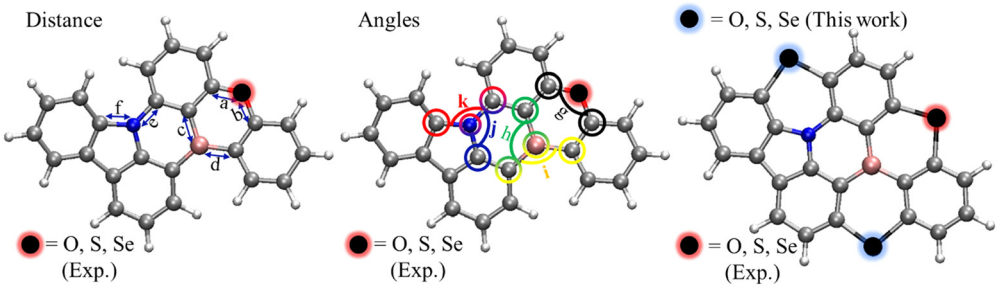

Fig. 2 Chemical structures of the **CzBX**: left distances, middle angles of **CzBX**, and right substitution of chalcogen (**CzBX2X**) atoms (X = O, S, or Se), see Table 1.

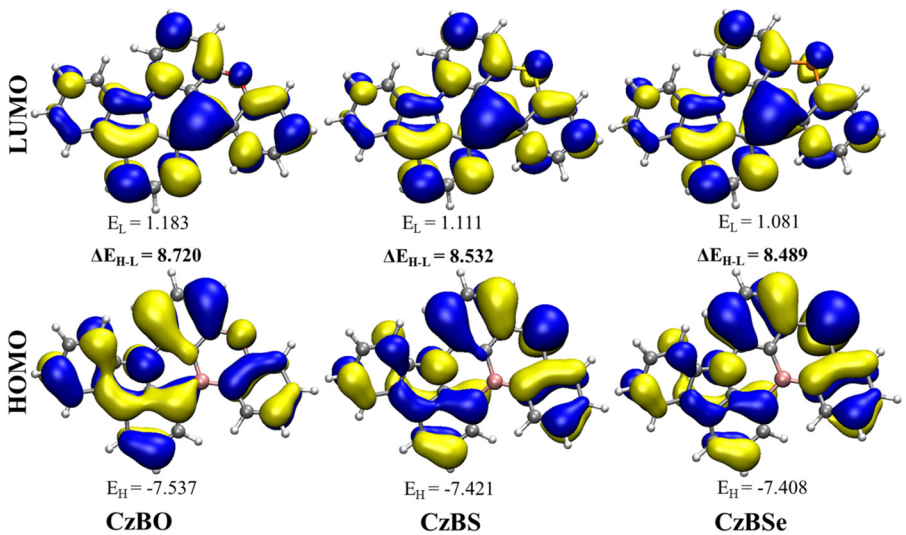

Fig. 3 HOMO and LUMO of **CzBX** (X = O, S, or Se) molecule (isosurface value is 0.02 a.u.). HOMO (E_H), LUMO (E_L) and energy gap (ΔE_{H-L}) energies are given in eV (obtained from the combined DFT-CCSD method).

are 441.8 nm (f = 0.3169) and 450.0 nm (f = 0.2881), respectively. This result is well comparable to the reported experimental values for **CzBX** (447 nm and 451 nm for S and Se substitution, respectively). These results show the importance of the combined DFT and CCSD method used in this work (see Table 2). Orbital configurations of the transitions are provided in Table S3 (ESI†). The combined DFT and CCSD method effectively reproduces the fluorescence data of the **CzBX** molecules. The calculated (experimental) fluorescence energies are 446.4 (445) nm, 468.3 (471) nm, and 476 (477) nm, respectively for O, S and Se substituted **CzBX** molecules, respectively (see Table 3).

Table 2 Calculated low energy optical absorption (in eV) spectra compared with different functionals and the experimental reported results (ref. 41)

Molecules	Expt.[41]	B3LYP	BHandHLYP	CAM-B3LYP	M062X	PBE0	ωb97xD	ω*B97XD	Combined DFT and CCSD
CzBO	2.910	3.036 f = 0.330	3.625 f = 0.488	3.520 f = 0.488	3.489 f = 0.476	3.138 f = 0.357	3.580 f = 0.507	3.427 f = 0.455	2.938 f = 0.342
CzBS	2.774	2.887 f = 0.301	3.476 f = 0.442	3.375 f = 0.413	3.334 f = 0.394	2.986 f = 0.324	3.435 f = 0.463	3.272 f = 0.413	2.806 f = 0.317
CzBSe	2.749	2.810 f = 0.274	3.418 f = 0.412	3.318 f = 0.444	3.270 f = 0.429	2.910 f = 0.296	3.380 f = 0.432	3.210 f = 0.383	2.755 f = 0.288
MAD*	0	0.100	0.695	0.593	0.554	0.200	0.654	0.492	**0.022**

$$*\mathrm{MAD} = \sum \frac{|\mathrm{Calc.} - \mathrm{Expt.}|}{n}.$$

Table 3 Comparison data of experimental (ref. 41) and theoretical absorption, emission profile data using the DFT-CCSD level of theory. f is the oscillator strength

	λ_{abs} ($S_0 \rightarrow S_1$) in nm		λ_F ($S_1 \rightarrow S_0$) in nm	
Molecules	Expt.	Cal.	Expt.	Cal.
CzBO	426	422.0 (f = 0.3415)	445	446.4 (f = 0.2985)
CzBS	447	441.8 (f = 0.3169)	471	468.3 (f = 0.2803)
CzBSe	451	450.0 (f = 0.2881)	477	476.0 (f = 0.2666)

3.3 Intersystem crossing and reverse intersystem crossing process

3.3.1 Origin of SOC and intersystem crossing (ISC). The interesting thing about light sources is that SOC depends on the structure, shape of the molecules and heavy atom effect, which will have a significant impact. Nowadays, organic molecule-based MR emitters are mostly constructed with heavy atoms (S, Se, Te and Br) and twisted-shape structures to achieve faster RISC rate constants for fluorescence. Additionally, the ΔE_{ST} plays a crucial role in fluorescence-based emitters. Both ΔE_{ST} and SOCME are important components in the overall TADF process. In this work, we explored a series of **CzBX** (X = O, S, Se) and substituted series of **CzBX2X**-based emitters. In the **CzBX** series of molecules, the fluorescence emission and delayed emission are purely dependent upon the puckered shape of the structure, heavy atoms and low ΔE_{ST}. The $\Delta E_{S_1-T_1}$ values decrease with an increase in the atomic number of the chalcogen atoms (0.155, 0.113 and 0.095 eV for O, S and Se-substituted **CzBX**, respectively). On the other hand, the experimentally reported $\Delta E_{S_1-T_1}$ values are 0.15, 0.11 and 0.12 eV for O, S and Se-substituted **CzBX**, respectively. The calculated $\Delta E_{S_1-T_1}$ values are well comparable with the reported experimental results (Table 4).

On the other hand, the $\Delta E_{S_1-T_2}$ increases with the chalcogen atom decreasing order (−0.054, −0.146 and −0.173 eV for O, S and Se-substituted **CzBX**, respectively). The negative $\Delta E_{S_1-T_2}$ value indicates that the T_2 state is higher in energy than the S_1 state. The $\Delta E_{S_1-T_n}$ energies between the S_1 and T_n (n = 1, 2) states and SOCME are reported in Tables 5 and 6 for the **CzBX** series. Based on the above ΔE_{ST} gap, we have calculated the rate constants of two possible transition ISC and RISC processes. Both the ISC and RISC process of MR-TADF emitters are greatly connected with the strength of SOC between the singlet and triplet states. In this study, for both **CzBX** and **CzBX2X** series, the strength of SOCME strongly depends on the excited state geometry and the presence of chalcogen atoms. Fig. 4 illustrates the top and side views, depicting the puckered shape for the **CzBX** series, the umbrella curve shape (UCS) for a few molecules, and the planar shape structure in the **CzBX2X** series (X = O, S, or Se). Also, the bond lengths (see Table S5, ESI†) increase in the same chalcogen order (O → S → Se). **CzBO** (d(C–O) is ∼1.36–1.37 Å), **CzBS** (d(C–S) is ∼1.75–1.76 Å), and **CzBSe** (d(C–Se) ∼1.87–1.89 Å) greatly increased this puckered shape structure, which helps to achieve the higher value of SOC matrix elements. For the ISC rate (k_{ISC}), SOCME is calculated in the geometry of S_1 for the ISC from $S_1 \rightarrow T_n$ (n = 1, 2) states. The SOCME between the S_1 and T_1 states increases with an increase in the atomic number of chalcogen atoms (0.086, 0.381 and 2.495 cm^{-1} for O, S, and Se-substituted **CzBX**, respectively). A similar observation was noted for the SOCME between the S_1 and T_2 states for **CzBX** molecules (0.099, 0.527 and 3.833 cm^{-1}, respectively). For the calculation of the RISC rate constants (k_{RISC}), the SOCMEs were calculated in the T_1 state optimized geometry for the $T_1 \rightarrow S_1$ RISC process and the T_2 state optimized geometry for the $T_2 \rightarrow S_1$ state RISC process. Similar to the SOCME for the ISC process, the SOCME for the RISC process increases with an increase in the atomic number of

Table 4 Calculated and experimental (ref. 41) $\Delta E_{S_1-T_1}$ (in eV) with different DFT functionals and CCSD methods

Molecules	Expt.	B3LYP	BHandHLYP	CAM-B3LYP	M062X	PBE0	ωb97xD	ω*B97XD	Combined DFT and CCSD
CzBO	0.15[a], 0.16[b]	0.46	0.87	0.73	0.60	0.51	0.67	0.55	0.155
CzBS	0.11[a], 0.14[b]	0.46	0.73	0.63	0.57	0.50	0.63	0.51	0.113
CzBSe	0.12[a], 0.15[b]	0.45	0.62	0.61	0.54	0.49	0.61	0.50	0.095
MAD	**0**	0.330	0.616	0.528	0.442	0.373	0.512	0.393	**0.011**

[a] Experimental values are measured in toluene. [b] Experimental values are measured in film state.The MAD value is calculated with respect to the experimental values obtained in toluene solvent. The tuned ω for ω*B97XD are provided in Table S1 (ESI).

Table 5 Calculated singlet–triplet energy difference (ΔE_{ST}), spin–orbit coupling matrix element (SOCME), and ISC rate constants (k_{ISC}) for the CzBX series

	ΔE_{ST}[a] (eV)		SOCME[a] (cm^{-1})		k_{ISC} (s^{-1})			Expt. [ref. 41] k_{ISC} (s^{-1})
Molecule	$S_1 \leftrightarrow T_1$	$S_1 \leftrightarrow T_2$	$S_1 \rightarrow T_2$	$S_1 \rightarrow T_2$	$S_1 \rightarrow T_1$	$S_1 \rightarrow T_2$	Total k_{ISC}	Toluene[b]/film[c]
CzBO	0.155	−0.054	0.086	0.099	3.86×10^6	2.45×10^5	0.4×10^7	—/2.5×10^7
CzBS	0.113	−0.146	0.381	0.527	5.79×10^7	4.74×10^5	0.6×10^8	2.1×10^8/1.9×10^8
CzBSe	0.095	−0.173	2.495	3.833	2.10×10^9	9.75×10^6	2.11×10^9	1.28×10^9/1.10×10^9

[a] ΔE_{ST} and SOCME were calculated using the combined DFT-CCSD method considering PCM (toluene) solvent. [b] Experimental ISC rate in toluene. [c] Experimental ISC rate in film.

Table 6 Calculated singlet–triplet energy difference (ΔE_{ST}), spin–orbit coupling matrix element (SOCME), and RISC rate constants (k_{RISC}) for the CzBX series

	ΔE_{ST}[a] (eV)		SOCME[a] (cm^{-1})		k_{RISC} (s^{-1})			Expt. [ref. 41] k_{RISC} (s^{-1})
Molecules	$S_1 \leftrightarrow T_1$	$S_1 \leftrightarrow T_2$	$S_1 \leftarrow T_1$	$S_1 \leftarrow T_2$	$S_1 \leftarrow T_1$	$S_1 \leftarrow T_2 \leftarrow T_1$[d]	Total k_{RISC}	Toluene[b]/film[c]
CzBO	0.155	−0.054	0.077	0.286	7.44×10^3	5.11×10^3	1.26×10^4	—/9×10^3
CzBS	0.113	−0.146	0.438	0.496	9.43×10^5	5.17×10^3	9.48×10^5	4×10^5/2.2×10^5
CzBSe	0.095	−0.173	2.209	4.054	4.08×10^7	2.6×10^5	0.41×10^8	1.5×10^8/1.8×10^8

[a] ΔE_{ST} and SOCME were calculated using the combined DFT-CCSD method considering the PCM (toluene) solvent. [b] Experimental ISC rate in toluene. [c] Experimental ISC rate in film. [d] The k_{RISC} values were calculated by taking into account the RISC from T_1 *via* T_2 to S_1; the relative population in the T_2 state with respect to that in the T_1 state was obtained by considering the thermal equilibrium (ref. 15).

chalcogen atoms (*viz.*, 0.077, 0.438 and 2.209 cm^{-1}, respectively, between the S_1 and T_1 states, see Table 6 and Table S5, ESI†). The ISC rate for the **CzBX** series is calculated using eqn (2)–(4) and compared with the available experimental data.[41] In this **CzBX** series of molecules, intramolecular H···H steric repulsions between the phenyl rings progressively increases, leading to the geometries becoming more puckered. This results in a twisted shape with heavy Se atoms, enhancing the spin–orbit coupling (SOC) and intersystem crossing rate (ISC and RISC) constants. The calculated ISC rate constants of **CzBO** and CzBS molecules are 4.0×10^6 s^{-1} and 6.0×10^7 s^{-1}, respectively. The same for the heavy chalcogen atom Se substituted in the **CzBSe** molecule is 2.11×10^9 s^{-1} and the corresponding reported experimental data is 1.28×10^9 s^{-1}. RISC is mostly favorable for this type of pure organic MR-TADF molecules. The k_{RISC} values were calculated by taking into account the RISC not only directly from T_1 to S_1 but also from T_1 to S_1 *via* the T_2 states. The relative population in the T_2 state with respect to that in the T_1 state was obtained by considering thermal equilibrium.[15]

The calculated rate constant of RISC for the **CzBO** molecule is 1.26×10^4 s^{-1}, while the reported experimental value is 9.0×10^3 s^{-1} (in film). For the **CzBS** molecule, the calculated and experimentally reported RISC rate constants are 9.48×10^5 s^{-1} and 4.0×10^5 s^{-1}, respectively. The heavy chalcogen atom Se substituted in the **CzBSe** molecule results in RISC rate constants of 0.41×10^8 s^{-1} (calc.) and 1.50×10^8 s^{-1} (exp.), respectively (see Table 6), which is the experimentally recorded high k_{RISC} in recent times.[41] The presence of heavy atoms gradually increased the k_{RISC} due to an increase in SOCME. In the **CzBX2X** series, the molecules are categorized into two types, *i.e.*, planar and UCS shape. The excited state geometry of these planar shapes has a 0° to 1.2° dihedral angle for **CzBO2S** (1.2°), **CzBO2Se** (0.4°), **CzBS2S** (0.1°), **CzBS2Se**, **CzBSe2S** and **CzBSe2Se**. The planar emitters have a very low SOCME, and in the presence of doubly substituted Se molecules with a high SOCME of above 0.088 cm^{-1} compared to other (non-Se atom and single substituted Se) SOCME of less than 0.009 cm^{-1} (except for **CzBSe2S**, 0.073 cm^{-1}). Similarly, the excited state geometry of UCS molecules is significantly increased (> 0.09 cm^{-1} due to the curve moiety). The dihedral angles of 20.8° (**CzBO2O**), 13.1° (**CzBS2O**), and 5.5° (**CzBSe2Se**) make the USC construction feasible, and the O atom has a shorter bond length with the nearest C atom distance (d(C–O) is ~1.37–1.4 Å), chalcogen has a longer bond length with the nearest C atom (C–O ~1.37–1.4 Å, C–S ~1.76 – 1.82 Å and C–Se ~1.92–1.99 Å), as shown in Table S6 (ESI†).

The UCS-shaped **CzBO2O** in the **CzBO2X** series has lower $\Delta E_{S_1-T_1}$ (= 0.043 eV) and comparatively higher SOCME (0.082 cm^{-1}) with a total ISC rate constant of 1.17×10^6 s^{-1}. Similarly, for RISC, **CzBO2O** has a higher value of SOCME ($S_1 \leftarrow T_1$ is 0.091 and $S_1 \leftarrow T_2$ is 0.213 cm^{-1}) and less energy gap ($\Delta E_{S_1-T_1}$ = 0.043, $E_{S_1-T_2}$ = −0.36 eV), and the conversional total RISC rate constant is 2.70×10^5 s^{-1}. The other two **CzBO2S** and **CzBO2Se** molecules are planar in nature due to the high S and Se atom distances, and the RMSD is also less than ~0.02 Å. The **CzBO2S** molecule has a lesser SOCME of 0.009 cm^{-1} and a smaller energy gap ($\Delta E_{S_1-T_1}$ = 0.028, $\Delta E_{S_1-T_2}$ = −0.075 eV), and the rate of RISC is 1.13×10^3 s^{-1}. The doubly substituted Se-based **CzBO2Se** molecule has a high SOCME (0.012 cm^{-1} in $S_1 \leftarrow T_1$ and 0.085 cm^{-1} in $S_1 \leftarrow T_2$) and increased the total k_{RISC} of 9.35×10^3 s^{-1}. In comparison, the **CzBO2X** series of rate ISC and RISC in **CzBO2O**, **CzBO2O** and **CzBO2Se** have high k_{ISC} (see Tables 7 and 8). In the **CzBS2X** series, the **CzBS2O** molecule, with a UCS, has less $\Delta E_{S_1-T_n}$ ($\Delta E_{S_1-T_1}$ is 0.137, $\Delta E_{S_1-T_2}$ is −0.196 eV) and high (in **CzBS2X** series only) SOCMEs

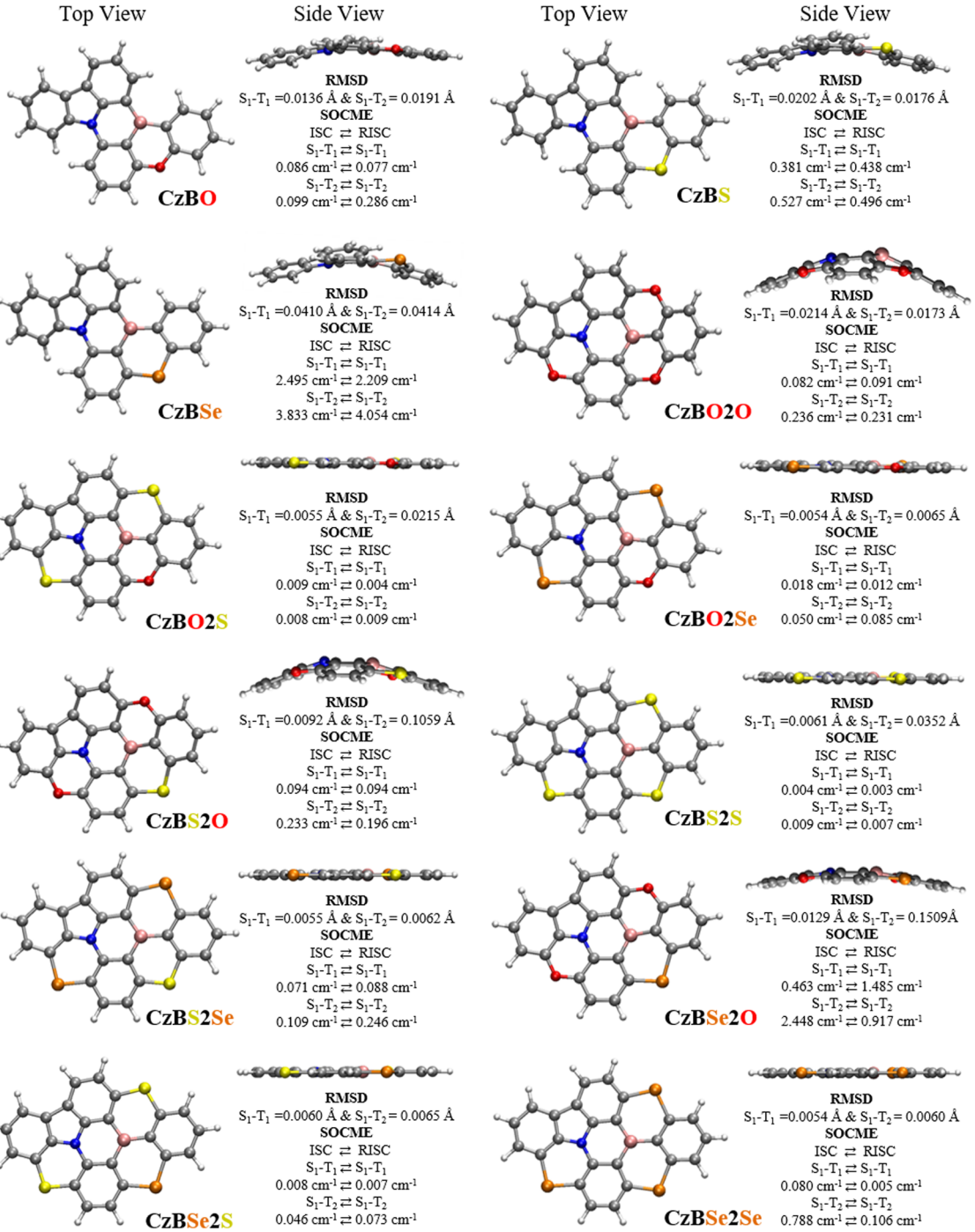

Fig. 4 The S_1 excited state structures of **CzBX** and **CzBX2X**. Excited state ($S_1/T_1/T_2$) different chalcogens bond distances with carbon atom (d(X–C) when X = O, S, or Se), collected in Table S6 (ESI†).

($S_1 \rightarrow T_1$ is 0.137 cm^{-1} and $S_1 \rightarrow T_2$ is 0.233 cm^{-1}); the conversional total ISC rate reached 4.22 × 10^6 s^{-1}. Similarly, for RISC, **CzBS2O** has a high SOCMEs ($S_1 \leftarrow T_1$ is 0.094 cm^{-1} and $S_1 \leftarrow T_2$ is 0.196 cm^{-1}) and less ($\Delta E_{S_1-T_1}$ = 0.137, $\Delta E_{S_1-T_2}$ = −0.196 eV) energy gap, and the total k_{RISC} reached 2.04 × 10^4 s^{-1}. The other two **CzBS2S** and **CzBS2Se** molecules are planar in nature. Also, these two molecules have low $\Delta E_{S_1-T_n}$ and SOCMEs; hence, their k_{ISC} becomes low as well as that of ~10^5 s^{-1}. The **CzBS2S** molecule has low SOC matrix elements ($S_1 \leftarrow T_1$ is 0.003 cm^{-1} and $S_1 \leftarrow T_2$ is 0.007 cm^{-1}), a smaller energy gap ($\Delta E_{S_1-T_1}$ = 0.086, $\Delta E_{S_1-T_2}$ = −0.129 eV), and the rate of RISC is 1.02 × 10^2 s^{-1}. For the **CzBS2Se** molecule, the heavy Se atom has a high SOCMEs ($S_1 \leftarrow T_1$ is 0.088 cm^{-1} and $S_1 \leftarrow T_2$ is 0.246 cm^{-1}), which increased the k_{RISC} up to 2.41 × 10^5 s^{-1}.

The ISC and RISC rates went up a lot because of the heavy Se atoms in the **CzBSe2X** series and the molecule **CzBSe2O**, which

Table 7 Calculated singlet–triplet energy difference (ΔE_{ST}), spin–orbit coupling matrix element (SOCME), and ISC rate constants (k_{ISC}) for **CzBX2X** molecules

Molecules	Calc. ΔE_{ST} (eV)		Calc. SOCME (cm^{-1})		k_{ISC} (s^{-1})		
	$S_1 \leftrightarrow T_1$	$S_1 \leftrightarrow T_2$	$S_1 \rightarrow T_1$	$S_1 \rightarrow T_2$	$S_1 \rightarrow T_1$	$S_1 \rightarrow T_2$	Tot. k_{ISC} (s^{-1})
CzBO2O	0.043	−0.360	0.082	0.236	1.17×10^6	7.60×10^0	1.17×10^6
CzBO2S	0.028	−0.075	0.009	0.008	1.11×10^4	9.32×10^2	1.20×10^4
CzBO2Se	0.013	−0.239	0.018	0.050	3.41×10^4	1.22×10^2	3.42×10^4
CzBS2O	0.137	−0.196	0.094	0.233	4.20×10^6	1.52×10^4	4.22×10^6
CzBS2S	0.086	−0.129	0.004	0.009	4.90×10^3	2.42×10^2	5.14×10^3
CzBS2Se	0.045	−0.275	0.071	0.109	9.03×10^5	1.17×10^2	9.04×10^5
CzBSe2O	0.207	−0.085	0.463	2.448	1.23×10^8	6.65×10^7	1.90×10^8
CzBSe2S	0.090	−0.208	0.008	0.046	2.05×10^4	3.72×10^2	2.09×10^4
CzBSe2Se	0.058	−0.240	0.080	0.788	1.38×10^6	2.91×10^4	1.41×10^6

Table 8 Calculated singlet–triplet energy difference (ΔE_{ST}), spin–orbit coupling matrix element (SOCME), and RISC rate constants (k_{RISC}) for **CzBX2X** molecules

Molecules	Calc. ΔE_{ST} (eV)		Calc. SOCME (cm^{-1})		k_{RISC} (s^{-1})		
	$S_1 \leftrightarrow T_1$	$S_1 \leftrightarrow T_2$	$S_1 \leftarrow T_1$	$S_1 \leftarrow T_2$	$S_1 \leftarrow T_1$	$S_1 \leftarrow T_2 \leftarrow T_1$	Tot. k_{RISC} (s^{-1})
CzBO2O	0.043	−0.360	0.091	0.213	2.70×10^5	1.17	2.70×10^5
CzBO2S	0.028	−0.075	0.004	0.009	7.36×10^2	3.97×10^2	1.13×10^3
CzBO2Se	0.013	−0.239	0.012	0.085	9.14×10^3	2.13×10^2	9.35×10^3
CzBS2O	0.137	−0.196	0.094	0.196	2.03×10^4	5.43×10^1	2.04×10^4
CzBS2S	0.086	−0.129	0.003	0.007	9.71×10^1	4.95	1.02×10^2
CzBS2Se	0.045	−0.275	0.088	0.246	2.41×10^5	1.04×10^2	2.41×10^5
CzBSe2O	0.207	−0.085	1.485	0.917	4.03×10^5	2.96×10^3	4.06×10^5
CzBSe2S	0.090	−0.208	0.007	0.073	4.73×10^2	2.93×10^1	5.02×10^2
CzBSe2Se	0.058	−0.240	0.089	0.106	1.79×10^5	5.52×10^1	1.79×10^5

has both UCS and heavy Se atoms. Among the **CzBX2X** series, **CzBSe2O** exhibited a high ISC rate due to its higher SOCMEs ($S_1 \rightarrow T_1$ is 0.463 cm^{-1} and $S_1 \rightarrow T_2$ is 2.448 cm^{-1}) value and the lowest energy gap ($\Delta E_{S_1\text{-}T_1}$ = 0.207 eV and $\Delta E_{S_1\text{-}T_2}$ = −0.085 eV). It reached a very high ISC rate constant of 1.9×10^8 s^{-1}. The RISC rate of **CzBSe2O** is the highest in the **CzBX2O** series, with a k_{RISC} of 4.06×10^5 s^{-1} due to its low energy gap and high SOC matrix elements ($S_1 \leftarrow T_1$ is 1.485 cm^{-1} and $S_1 \leftarrow T_2$ is 0.917 cm^{-1}). The other two molecules are planar with the heavy Se atom of **CzBSe2S** as the low energy gap and a low SOCMEs ($S_1 \rightarrow T_1$ is 0.008 cm^{-1} and $S_1 \rightarrow T_2$ is 0.046 cm^{-1}) value to reach k_{ISC} of 2.09×10^4 s^{-1}. But the RISC rate in **CzBSe2S** (single Se and double S atom) is low SOCMEs (in $S_1 \leftarrow T_1$ is 0.007 cm^{-1} and $S_1 \leftarrow T_2$ is 0.073 cm^{-1}) value to achieve 5.02×10^2 s^{-1}. The **CzBSe2Se** molecule with three Se atoms and planar geometry has lower rate (ISC and RISC) constants (see Tables 7 and 8). The **CzBSe2Se** molecule has a low energy gap ($\Delta E_{S_1\text{-}T_1}$ = 0.058, $\Delta E_{S_1\text{-}T_2}$ = −0.240 eV) and good SOC matrix elements ($S_1 \rightarrow T_2$ is 0.788 cm^{-1}) to increase the k_{ISC} up to 1.41×10^6 s^{-1}. The rate of RISC also had good SOCMEs ($S_1 \leftarrow T_1$ is 0.089 and $S_1 \leftarrow T_2$ is 0.106 cm^{-1}) to achieve the k_{RISC} up to 1.79×10^5 s^{-1}. The highest RISC rate constant for the **CzBSe2Se** molecule, as reported in a previous work by Pratik *et al.*,[47,48] showed that increasing the chalcogen heavy Se atom greatly increases the RISC rate constants for non-planar molecules, but in our study, due to the planar geometry (0° dihedral angle) with triple Se heavy atoms, the k_{RISC} becomes $\sim 10^5$ s^{-1}.

The RISC values are higher for doubly substituted chalcogen atoms: 2.7×10^5 s^{-1}, 2.04×10^4 s^{-1} and 4.06×10^5 s^{-1} for **CzBO2O**, **CzBS2O** and **CzBSe2O**, respectively, due to the UCS shape (high bond distance in C–Se and less bond distance in

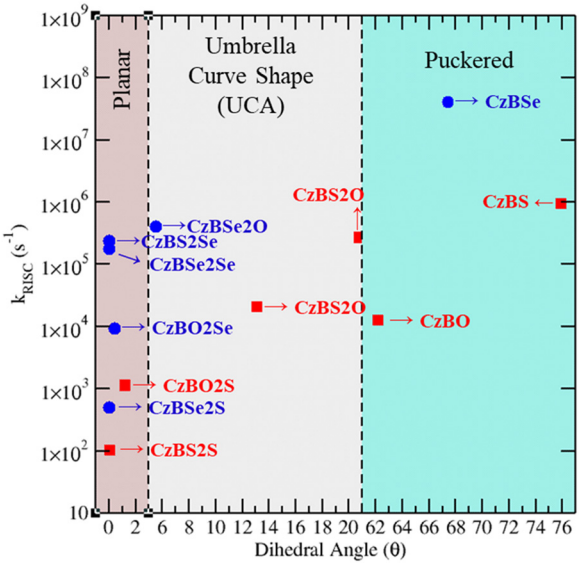

Fig. 5 The effect of dihedral angle in MR-TADF and how it affects the RISC rate constants in different shapes (planar (brown), UCS (grey) and puckered (turquoise)). Here, blue and red circles denote the molecules with and without Se atoms in both **CzBX** and **CzBX2X**.

Table 9 Comparison of the calculated rate constant for fluorescence (k_F), ISC (k_{ISC}) and RISC (k_{RISC}) processes in s^{-1} (here, ϕ is the dihedral angle in degrees)

	O				S				Se			
Molecules	ϕ (°)	k_F (10^7)	k_{ISC} (10^7)	k_{RISC} (10^4)	ϕ (°)	k_F (10^7)	k_{ISC} (10^7)	k_{RISC} (10^4)	ϕ (°)	k_F (10^7)	k_{ISC} (10^7)	k_{RISC} (10^5)
CzBX (expt.)	—	15/13	—/2.5	—/0.9	—	1.5/3.3	21/19	40/22	—	0.05	128/110	1500/1800
CzBX	62.2	17.4	0.41	1.26	75.9	15	5.84	94.8	67.4	14.6	211	411
CzBO2X	20.8	11.4	0.17	27	1.2	9	1.2×10^4	0.13	0.4	9.13	3.42×10^4	0.093
CzBS2X	13.1	12.2	0.42	2.04	0.1	9.24	5.1×10^3	1.02×10^2	0	8.51	0.09	2.41
CzBSe2X	5.5	14.2	19	4.06	0	8.62	2.1×10^4	5.02×10^2	0	8.33	0.14	6.21×10^2

C–O, see Table S5 for the UCS, ESI†) moiety. The majority of heavy atom compounds in MR-TADF reached the k_{RISC}, which is approximately 10^{4-7} s^{-1}.[71–73] This study shows the lightest atom with UCS, resulting in a k_{RISC} $\sim 10^5$ s^{-1} for the **CzBX2O** series. The natural transition orbitals (NTOs) presented in Fig. S2 (ESI†) shows the intramolecular charge transfer nature. The rate of emission can decide the path; taking a deep look into the k_F and k_P decides the best way of converting the exciton energy of $S_1 \rightleftarrows T_n$ (ISC and RISC) to reach ~100% of IQE.

3.3.2 Dihedral angle *vs.* RISC rate constants. The dihedral angles of **CzBX** and **CzBX2X** series are calculated in the C–N–B–C middle part (see Fig. 4). The dihedral angle and SOCME are the major phenomena that enhance the RISC rate constants plotted in Fig. 5. The shapes of molecules are described using different layer colours. The planar (unsubstituted Se atom) structure, having lower SOCME values ~0.009 cm^{-1} (in $S_1 \leftarrow T_1$ and $S_1 \leftarrow T_2$), reached the RISC rate constants lower than 10^3 s^{-1}. Similarly, the similar planar structure with Se atom molecules reached the highest RISC rate up to 10^3–10^5 s^{-1} (**CzBO2Se**, **CzBS2Se** and **CzBSe2Se**), and the dihedral angle is 1.2° for **CzBO2S** (due to the O distance, see Table S5, ESI†) while **CzBS2S** is planar (see Fig. 4). The UCS structure has a high RISC rate constant due to the non-planar shape and dihedral angle of 20.8° for **CzBO2O** (triple O atom high dihedral angle in **CzBX2X** series), 13.1° for **CzBS2O** and 5.5° for **CzBSe2O**. These dihedral angles boosted the SOCME values and hence increased the RISC rate constants up to 10^4–10^5 s^{-1}. The main series of **CzBX** has a puckered shape and is twisted in the excited state; the dihedral angle also greatly increases in the 62°–76° range. High dihedral angle increases the SOCME and RISC rate constants up to 1.26×10^4 s^{-1} (**CzBO**), 9.48×10^5 s^{-1} (**CzBS**), and 0.41×10^8 s^{-1}(**CzBSe**). The presence of heavy or metal atoms will significantly increase the intersystem rate constants (ISC and RISC), and SOCME always plays an important role in the twisted or bent shape of the structure.

The different rate constants of fluorescence (k_F), ISC (k_{ISC}) and RISC (k_{RISC}) are compared in Table 9 (and Table S7, ESI†). Because of the higher rate constant for RISC compared to that of phosphorescence, these molecules show TADF features (see Fig. 6).

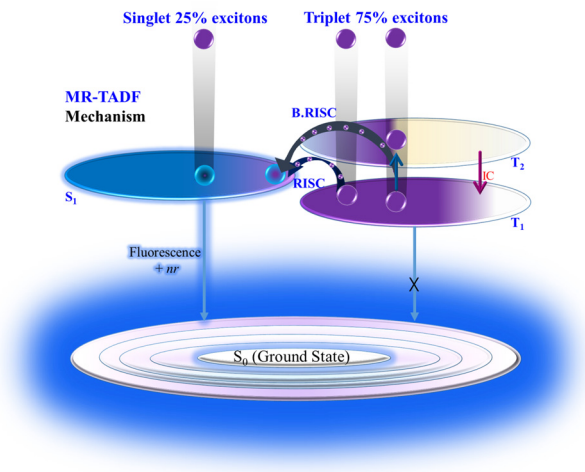

Fig. 6 MR-TADF mechanism in harvesting triplet excitons. Here B. RISC is T_1 to S_1 conversion *via* the T_2 state. The relative population in the T_2 state compared with the T_1 state was obtained by considering thermal equilibrium (using the Boltzmann factor).

4. Conclusions

In conclusion, we investigated how chalcogens (O → S → Se) affect the MR-TADF features and properties for a series of **CzBX** and **CzBX2X** molecules obtained either by the substitution of O atoms with S or Se in **CzBX** or by fusing intramolecular H···H bond with chalcogen atoms, the **CzBX** adjacent phenyl position to create the new MR-TADF **CzBX2X** series. The results of calculations based on highly correlated wave functions show the following.

(i) The **CzBX** and **CzBX2X** series of MR-TADF emitters have high radiative (fluorescence) rate constants (k_F) of about ~10^{7-8} s^{-1}.

(ii) The ISC and RISC rate constants that follow are significantly influenced by the molecules electronic structure and geometry. While the **CzBX** series has the same chemical compositions, the ISC and RISC rate constants are found to be much larger due to the increasing chalcogen molecular size order (O → S → Se) compared to the **CzBX2X** series, which has lower SOCME values due to the planer and puckered geometry. UCS structures have higher SOCMEs.

(iii) The selenium-containing (**CzBX**) molecules exhibit higher ISC and RISC rate values (k_{ISC} ~ 10^9 s^{-1} and k_{RISC} ~ 10^8 s^{-1}), which is due to the higher spin–orbit coupling interactions. The higher RISC rate constants in the **CzBX2X** series for both types of planar and UCS geometries reach ~10^5 s^{-1}.

(iv) The phosphorescence rate constants (k_P) are in the range from $\sim 10^1$ to 10^4 s^{-1} (calculated). Due to faster RISC and fluorescence rate constants, these **CzBX** and **CzBX2X** series of MR-TADF emitters show bright fluorescence ($k_F \sim 10^{7-8}$ s^{-1}).

(v) This **CzBX** series of molecules has a unique deep-sky blue luminescence with sharp narrow band emission peaks and **CzBX2X** as bright bluish emitters.

Overall, we demonstrated that the chemical nature of the chalcogen atoms, as well as their changing position(s), have a significant influence on the optical and electronic features of the **CzBX** and **CzBX2X**-based MR-TADF emitters and their accurate prediction using combined DFT and CCSD methods. We compared our calculated results with available experimentally reported data to validate our computational methodology used in this study. We used PCM solvent (toluene) model to mimic the surrounding environment effect in the bulk. In reality, it is difficult to mimic the properties of thin films as the properties of any thin-film depend on its thickness. Here in, we explained the origins of MR-TADF properties in organoboron heteroatom-embedded molecules from the molecular point of view. We believe that the present methodology and findings will aid in the development of narrow-band blue OLED emitters with a high level of efficiency.

Author contributions

P. S.: conceptualization of the total work, computation and analysis of the works done, writing the original manuscript. P. K. S.: overall supervision, analysis and writing the manuscript.

Conflicts of interest

The authors declare no competing financial interest.

Acknowledgements

P. S. thanks BITS-Pilani for the ''Institute Research Fellowship''. P. K. S. thanks Department of Science and Technology-Science and Engineering Research Board (DST-SERB), Government of India (grant number: CRG/2021/002706) for the partial financial support. We acknowledge the support for high-performance computing and storage resources at GITAM and BITS-Pilani (Hyderabad Campus).

References

1 T. Wang, Y. Zou, Z. Huang, N. Li, J. Miao and C. Yang, *Angew. Chem., Int. Ed.*, 2022, **61**, 1–7.
2 H. Gao, S. Shen, Y. Qin, G. Liu, T. Gao, X. Dong, Z. Pang, X. Xie, P. Wang and Y. Wang, *J. Phys. Chem. Lett.*, 2022, **13**, 7561–7567.
3 S. Lin, Z. Pei, B. Zhang, H. Ma and W. Z. Liang, *J. Phys. Chem. A*, 2022, **126**, 239–248.
4 P. Jiang, J. Miao, X. Cao, H. Xia, K. Pan, T. Hua, X. Lv, Z. Huang, Y. Zou and C. Yang, *Adv. Mater.*, 2022, **34**, 1–7.
5 Y. C. Cheng, X. C. Fan, F. Huang, X. Xiong, J. Yu, K. Wang, C. S. Lee and X. H. Zhang, *Angew. Chem., Int. Ed.*, 2022, **61**, 1–6.
6 X. Wu, J. Huang, B. Su, S. Wang, L. Yuan, W. Zheng, H. Zhang, Y. Zheng, W. Zhu and P. Chou, *Adv. Mater.*, 2022, **34**, 2270006.
7 G. Zhao, D. Liu, P. Wang, X. Huang, H. Chen, Y. Zhang, D. Zhang, W. Jiang, Y. Sun and L. Duan, *Angew. Chem., Int. Ed.*, 2022, **61**, e202212861.
8 J. Park, J. Lim, J. H. Lee, B. Jang, J. H. Han, S. S. Yoon and J. Y. Lee, *ACS Appl. Mater. Interfaces*, 2021, **13**, 45798–45805.
9 Y. Liu, X. Xiao, Z. Huang, D. Yang, D. Ma, J. Liu, B. Lei, Z. Bin and J. You, *Angew. Chem., Int. Ed.*, 2022, **134**, e202210210.
10 N. Ikeda, S. Oda, R. Matsumoto, M. Yoshioka, D. Fukushima, K. Yoshiura, N. Yasuda and T. Hatakeyama, *Adv. Mater.*, 2020, **32**, 1–6.
11 W. Sotoyama, *J. Phys. Chem. A*, 2021, **125**, 10373–10378.
12 S. Wu, W. Li, K. Yoshida, D. Hall, S. Madayanad Suresh, T. Sayner, J. Gong, D. Beljonne, Y. Olivier, I. D. W. Samuel and E. Zysman-Colman, *ACS Appl. Mater. Interfaces*, 2022, **14**, 22314–22352.
13 H. Cheon, S. Woo, S. Baek, J. Lee and Y. Kim, *Adv. Mater.*, 2022, **34**, 2207416.
14 P. K. Samanta and N. J. English, *J. Phys. Chem. C*, 2020, **124**, 8178–8185.
15 P. K. Samanta, D. Kim, V. Coropceanu and J. L. Brédas, *J. Am. Chem. Soc.*, 2017, **139**, 4042–4051.
16 B. C. Garain, P. K. Samanta and S. K. Pati, *J. Phys. Chem. A*, 2021, **125**, 6674–6680.
17 S. Kuila, A. Ghorai, P. K. Samanta, R. B. K. Siram, S. K. Pati, K. S. Narayan and S. J. George, *Chem. – Eur. J.*, 2019, **25**, 16007–16011.
18 H. Shu, L. Chen, X. Wu, T. Wang, S. Wang, H. Tong and L. Wang, *J. Mater. Chem. C*, 2022, **10**, 1833–1838.
19 B. Li, Z. Yang, W. Gong, X. Chen, D. W. Bruce, S. Wang, H. Ma, Y. Liu, W. Zhu, Z. Chi and Y. Wang, *Adv. Opt. Mater.*, 2021, **9**, 1–10.
20 P. Sivasakthi, J. M. Jacob, M. K. Ravva and P. K. Samanta, *J. Phys. Chem. A*, 2022, **124**, 886–893.
21 A. Arjona-Esteban, S. Barbara and O. Julian, *Lumin. OLED Technol. Appl.*, 2019, 1–18.
22 D. K. A. Phan Huu, S. Saseendran, R. Dhali, L. G. Franca, K. Stavrou, A. Monkman and A. Painelli, *J. Am. Chem. Soc.*, 2022, **144**, 15211–15222.
23 R. Dhali, D. K. A. Phan Huu, F. Terenziani, C. Sissa and A. Painelli, *J. Chem. Phys.*, 2021, **154**, 134112.
24 M. Li, W. Xie, X. Cai, X. Peng, K. Liu, Q. Gu, J. Zhou, W. Qiu, Z. Chen, Y. Gan and S. J. Su, *Angew. Chem., Int. Ed.*, 2022, **61**, e202209343.
25 A. Chatterjee, J. Chatterjee, S. Sappati, T. Sheikh, R. M. Umesh, M. D. Ambhore, M. Lahiri and P. Hazra, *J. Phys. Chem. B*, 2021, **125**, 12832–12846.
26 Kenry, C. Chen and B. Liu, *Nat. Commun.*, 2019, **10**, 1–15.
27 J. Yu, H. Ma, W. Huang, Z. Liang, K. Zhou, A. Lv, X.-G. Li and Z. He, *JACS Au*, 2021, **1**, 1694–1699.
28 P. K. Samanta and S. K. Pati, *J. Mol. Model.*, 2018, **24**, 1–11.

29 N. Liang, G. Liu, D. Hu, K. Wang, Y. Li, T. Zhai, X. Zhang, Z. Shuai, H. Yan, J. Hou and Z. Wang, *Adv. Sci.*, 2022, **9**, 2103975.
30 R. K. Konidena and K. R. Naveen, *Adv. Photonics Res.*, 2022, **3**, 2200201.
31 K. R. Naveen, P. Palanisamy, M. Y. Chae and J. H. Kwon, *Chem. Commun.*, 2023, **59**, 3685–3702.
32 T. Wang, A. K. Gupta, D. B. Cordes, A. M. Z. Slawin and E. Zysman-Colman, *Adv. Opt. Mater.*, 2023, **11**, 2300114.
33 T. Hatakeyama, K. Shiren, K. Nakajima, S. Nomura, S. Nakatsuka, K. Kinoshita, J. Ni, Y. Ono and T. Ikuta, *Adv. Mater.*, 2016, **28**, 2777–2781.
34 S. Madayanad Suresh, D. Hall, D. Beljonne, Y. Olivier and E. Zysman-Colman, *Adv. Funct. Mater.*, 2020, **30**, 1908677.
35 S. Oda, W. Kumano, T. Hama, R. Kawasumi, K. Yoshiura and T. Hatakeyama, *Angew. Chem.*, 2021, **133**, 2918–2922.
36 K. R. Naveen, H. I. Yang and J. H. Kwon, *Commun. Chem.*, 2022, **5**, 149.
37 S. Oda, T. Sugitani, H. Tanaka, K. Tabata, R. Kawasumi and T. Hatakeyama, *Adv. Mater.*, 2022, **34**, 1–6.
38 K. R. Naveen, H. Lee, L. H. Seung, Y. H. Jung, C. P. Keshavananda Prabhu, S. Muruganantham and J. H. Kwon, *Chem. Eng. J.*, 2023, **451**, 138498.
39 P. Palanisamy, O. P. Kumar, H. U. Kim, K. R. Naveen, J. Y. Kim, J. H. Baek, M. Y. Chae and J. H. Kwon, *Chem. Eng. J.*, 2024, **481**, 148781.
40 H. X. Ni, X. F. Luo, L. Yuan, J. J. Hu, W. W. Zhang and Y. X. Zheng, *J. Mater. Chem. C*, 2024, **12**, 2578–2584.
41 I. S. Park, H. Min and T. Yasuda, *Angew. Chem., Int. Ed.*, 2022, **134**, e202205684.
42 M. Yang, I. S. Park and T. Yasuda, *J. Am. Chem. Soc.*, 2020, **142**, 19468–19472.
43 Y. Zhang, D. Zhang, J. Wei, Z. Liu, Y. Lu and L. Duan, *Angew. Chem., Int. Ed.*, 2019, **58**, 16912–16917.
44 K. Matsui, S. Oda, K. Yoshiura, K. Nakajima, N. Yasuda and T. Hatakeyama, *J. Am. Chem. Soc.*, 2018, **140**, 1195–1198.
45 H. Hirai, K. Nakajima, S. Nakatsuka, K. Shiren, J. Ni, S. Nomura, T. Ikuta and T. Hatakeyama, *Angew. Chem., Int. Ed.*, 2015, **54**, 13581–13585.
46 H. Jiang, Y. Cao, Q. Yang, L. Xian, Y. Tao, R. Chen and W. Huang, *J. Phys. Chem. Lett.*, 2020, **11**, 7739–7754.
47 S. M. Pratik, V. Coropceanu and J. L. Brédas, *Chem. Mater.*, 2022, **34**, 8022–8030.
48 S. M. Pratik, V. Coropceanu and J. L. Brédas, *ACS Mater. Lett.*, 2022, **4**, 440–447.
49 H. Sun, C. Zhong and J. L. Brédas, *J. Chem. Theory Comput.*, 2015, **11**, 3851–3858.
50 M. Rubešová, E. Muchová and P. Slavíček, *J. Chem. Theory Comput.*, 2017, **13**, 4972–4983.
51 G. Scalmani and M. J. Frisch, *J. Chem. Phys.*, 2010, **132**, 114110.
52 S. Rohman and R. Kar, *J. Phys. Chem. A*, 2022, **126**, 3452–3462.
53 O. S. Bokareva, G. Grell, S. I. Bokarev and O. Kühn, *J. Chem. Theory Comput.*, 2015, **11**, 1700–1709.
54 L. Kronik, T. Stein, S. Refaely-Abramson and R. Baer, *J. Chem. Theory Comput.*, 2012, **8**, 1515–1531.
55 M. J. Frisch, G. W. Trucks, H. B. Schlegel, G. E. Scuseria, M. A. Robb, J. R. Cheeseman, G. Scalmani, V. Barone, G. A. Petersson, H. Nakatsuji, X. Li, M. Caricato, A. V. Marenich, J. Bloino, B. G. Janesko, R. Gomperts, B. Mennucci, H. P. Hratchian, J. V. Ortiz, A. F. Izmaylov, J. L. Sonnenberg, D. Williams-Young, F. Ding, F. Lipparini, F. Egidi, J. Goings, B. Peng, A. Petrone, T. Henderson, D. Ranasinghe, V. G. Zakrzewski, J. Gao, N. Rega, G. Zheng, W. Liang, M. Hada, M. Ehara, K. Toyota, R. Fukuda, J. Hasegawa, M. Ishida, T. Nakajima, Y. Honda, O. Kitao, H. Nakai, T. Vreven, K. Throssell, J. A. Montgomery, Jr., J. E. Peralta, F. Ogliaro, M. J. Bearpark, J. J. Heyd, E. N. Brothers, K. N. Kudin, V. N. Staroverov, T. A. Keith, R. Kobayashi, J. Normand, K. Raghavachari, A. P. Rendell, J. C. Burant, S. S. Iyengar, J. Tomasi, M. Cossi, J. M. Millam, M. Klene, C. Adamo, R. Cammi, J. W. Ochterski, R. L. Martin, K. Morokuma, O. Farkas, J. B. Foresman and D. J. Fox, *Gaussian 16, Revision C.02*, Gaussian, Inc., Wallingford CT, 2016.
56 A. Pershin, D. Hall, V. Lemaur, J. C. Sancho-Garcia, L. Muccioli, E. Zysman-Colman, D. Beljonne and Y. Olivier, *Nat. Commun.*, 2019, **10**, 597.
57 F. Neese, F. Wennmohs, U. Becker and C. Riplinger, *J. Chem. Phys.*, 2020, **152**, 224108.
58 F. Neese, *Wiley Interdiscip. Rev.: Comput. Mol. Sci.*, 2022, **12**, e1606.
59 F. Weigend and R. Ahlrichs, *Phys. Chem. Chem. Phys.*, 2005, **7**, 3297–3305.
60 A. K. Dutta, M. Nooijen, F. Neese and R. Izsák, *J. Chem. Phys.*, 2017, **146**, 074103.
61 V. Lawetz, G. Orlandi and W. Siebrand, *J. Chem. Phys.*, 1972, **56**, 4058–4072.
62 G. W. Robinson and R. P. Frosch, *J. Chem. Phys.*, 1963, **38**, 1187–1203.
63 K. Schmidt, S. Brovelli, V. Coropceanu, D. Beljonne, J. Cornil, C. Bazzini, T. Caronna, R. Tubino, F. Meinardi, Z. Shuai and J. L. Brédas, *J. Phys. Chem. A*, 2007, **111**, 10490–10499.
64 R. C. Hilborn, *Am. J. Phys.*, 1982, **50**, 982–986.
65 E. Jansson, B. Minaev, S. Schrader and H. Ågren, *Chem. Phys.*, 2007, **333**, 157–167.
66 Q. Zhang, X. Wang, Y. Zhang, L. Wang, J. Li and J. Zhang, *J. Phys. Chem. C*, 2016, **120**, 27523–27532.
67 Z. Shuai and Q. Peng, *Phys. Rep.*, 2014, **537**, 123–156.
68 M. T. do Casal, K. Veys, M. H. E. Bousquet, D. Escudero and D. Jacquemin, *J. Phys. Chem. A*, 2023, **127**, 10033–10053.
69 A. Manian and S. P. Russo, *Sci. Rep.*, 2022, **12**, 21481.
70 M. H. E. Bousquet, T. V. Papineau, K. Veys, D. Escudero and D. Jacquemin, *J. Chem. Theory Comput.*, 2023, **19**, 5525–5547.
71 X. Cao, K. Pan, J. Miao, X. Lv, Z. Huang, F. Ni, X. Yin, Y. Wei and C. Yang, *J. Am. Chem. Soc.*, 2022, **144**, 22976–22984.
72 S. Wu, L. Zhang, J. Wang, A. Kumar Gupta, I. D. W. Samuel and E. Zysman-Colman, *Angew. Chem., Int. Ed.*, 2023, **62**, e202305182.
73 T. Wang, A. K. Gupta, D. B. Cordes, A. M. Z. Slawin and E. Zysman-Colman, *Adv. Opt. Mater.*, 2023, **11**, 2300114.